Accounting for mesoscale geometry and intra-yarn fiber volume fraction distribution on 3D angle-interlock fabric permeability, International Journal of Multiphase Flow

Morgan Cataldi, Yanneck Wielhorski, Nicolas Moulin, Augustin Parret-Fréaud, Monica Francesca Pucci, Pierre-Jacques Liotier

Accounting for mesoscale geometry and intra-yarn fiber volume fraction distribution on 3D angle-interlock fabric permeability

Morgan Cataldi[a,b], Yanneck Wielhorski[b], Nicolas Moulin[a,*], Augustin Parret-Fréaud[c], Monica Francesca Pucci[d], Pierre-Jacques Liotier[e]

[a] *Mines Saint-Étienne, Université de Lyon, CNRS, UMR 5307 LGF, 158 Cours Fauriel 42023, Saint-Étienne, France*
[b] *Safran Aircraft Engines, Rond-point René Ravaud - Réau, 77550 Moissy-Cramayel, France*
[c] *Safran Tech, Rue des Jeunes Bois, 78772 Magny-les-Hameaux, France*
[d] *LMGC, IMT Mines Ales, Univ Montpellier, CNRS, Ales, France*
[e] *Polymers Composites and Hybrids (PCH), IMT Mines Alès, Alès, France*

Abstract

Understanding resin flows within 3D interlock fabrics involves addressing a dual-scale flow problem. Indeed, the fluid can flow through inter-yarn channels, characterized by a unit cell mesoscale morphology, but also within yarns considered as homogeneous equivalent porous media. The former is assumed to follow the Stokes' law while the latter be related to the Darcy's law, directly linked to the microscopic intra-yarn fiber volume fraction (FVF) field. In this work, a coupled Stokes-Darcy steady-state flow within a 3D woven textile, modeled at mesoscale, is solved through a finite element monolithic approach with a mixed velocity-pressure formulation, stabilized by the Variational MultiScale Method (VMS) and implemented in the Z-set software. The fabric permeability tensor is then computed without any assumptions on its nature and analyzed both through its diagonal components, its eigenvectors and eigenvalues. The main contribution of this study lies in examining the influence of variations of the inter-yarn porous medium morphology, through textile compaction and geometrical reduction to prevent edge flows, and the intra-yarn permeability (from complete field to unique value) on the overall fabric permeability.

Keywords: **Textile composites, Material modeling, Resin Transfer Moulding (RTM), Numerical flow simulations, Finite Element Analysis (FEA), Stokes-Darcy coupling, Permeability**

*Corresponding author.
Email address: nicolas.moulin@emse.fr (Nicolas Moulin)

1. Introduction

Composite parts are used in various industrial fields, and among them in aeronautics within aircraft engines [1]. The wide range of applications in which composite materials are used leads therefore to a large variety of materials and their associated manufacturing processes [2]. The material addressed in this study is a 3D angle-interlock fabric used within aircraft engines blades and manufactured through Resin Transfer Molding (RTM) process. Dry preforms are produced by weaving twisted carbon fiber yarns and interlacing warp and weft yarn layers [3]. The first step of the RTM process consists in compacting the preform within a mold to reach the desired global fiber volume fraction (FVF) [4]. The second one consists in the impregnation of the compacted preform by a resin at liquid state.

Mechanical behavior of the manufactured composite parts is highly related to impregnation defects characterized by the size and morphology of dry areas or voids within the preform [5, 6]. These are formed during the impregnation step and are linked both to process parameters [7, 8] and to the preform **conductance for liquid flow** [9]. This characteristic is the permeability K, firstly introduced by Darcy to link the flow rate to the pressure drop within a porous medium for an unidirectional saturated fluid flow. The original Darcy's law can be extended to 3D models thanks to homogenisation theory [10], but its unidirectional flow rate formulation is still widely used [11, 12]. Several benchmarks **carried out** on both in-plane [13–15] and transverse permeability [16] showed various experimental setups and techniques to determine a permeability value. However, they have also highlighted the complexity of permeability characterization which comes from various distortions of the preform during its processing [17, 18]. As a consequence, new **virtual** methods of predicting a composite material permeability have been developed such as an idealisation of the pore network into rectangular channels [19, 20] or the use of artificial intelligence algorithms [21, 22]. **The computation of the fabric effective permeability tensor K_{eff} in the present work follows the conclusions presented in [23] by not assuming it to be oriented along the weaving pattern directions.** The term permeability refers in this study to the saturated permeability characterized for a steady-state flow across the porous medium. It differs from the unsaturated permeability which is characterized for a transient flow across the porous medium [24].

Because of the multi-scale nature of the 3D angle-interlock fabrics, an accurate characterization of the composite reinforcement permeability should be performed at every scale as shown in Figure 1. Indeed, the permeability of the whole part cannot be determined. Consequently, the permeability characterization at the lower scales could help for filling macroscale simulations. As such, several works are devoted to a dual length scale permeability charac-

terization on *(i)* preforms at the mesoscale (3D or stacked prepregs) [25–27] or *(ii)* a single yarn at the microscale [27–32]. In between, working at the mesoscopic scale with homogenised intra-yarn features allowed to study their effect on the fabric permeability without modeling the thousands of carbon fibers they contain [33]. The mesoscopic woven modeling of unit cells used in numerical simulations come from various approaches [34]. On one part, manufactured preform can be described through X-Ray microtomography acquisition (μ-CT) [35–37] for example. On the another part, a textile modeling software such as WiseTex [38], TexGen [39] or Multifil [40, 41] can predict the resulting textile unit cell. Recently, artificial intelligence [42–44] has also been employed for predicting its mesoscopic yarn morphology.

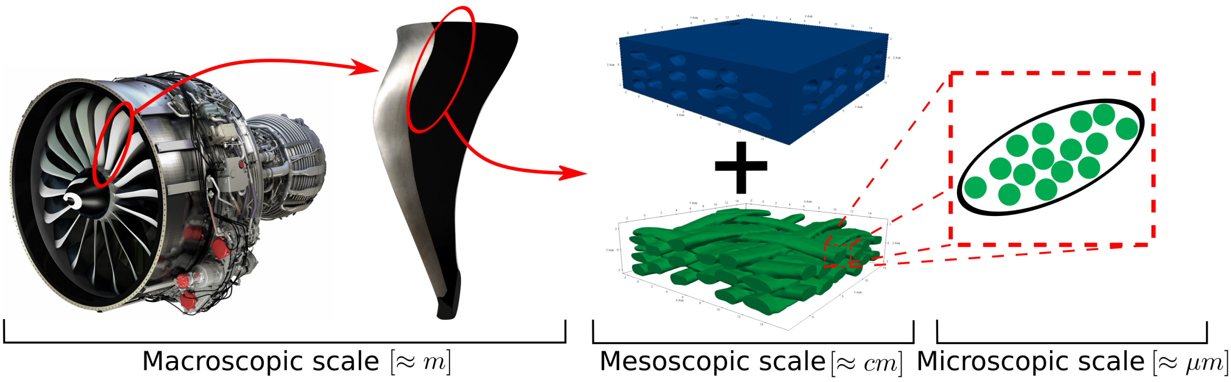

Figure 1: Left to right: from aircraft engine to composite blade[1], 3D interlock unit cell (**resin** + **yarns**) and carbon fibers within a tow.

The dual-scale steady state fluid flow is commonly modeled by Stokes' equation between the yarns and Brinkman's equation within them. It is consistent because the viscous dissipation term in both equations ensures the velocity and stress continuity at the interface, and is thus used in many works [45–47]. However, this model faces numerical issues for very low intra-yarn permeability values such as in [48], thus a Stokes-Darcy coupled model is used in the present study. Different numerical strategies can be used to solve the steady-state fluid flow problem within a 3D woven fabric unit cell. The Finite Element Method (FEM) [49, 50], the Lattice Boltzmann Method (LBM) [45], the asymptotic homogenization technique [51], the phase field method [52], the Proper Generalized Decomposition technique (PGD) [47] and the Dual-Scale Skeleton model (DSS) [53] are some of them. The strategy applied here is a Finite Element (FE) monolithic approach with a mixed velocity-pressure formulation and the Variational MultiScale (VMS) approach as a stabilization technique to solve the Stokes-Darcy coupled problem [54–56]. Numerical studies have investigated the dependencies of a 3D woven fabric permeability on several of its inner variations, both

[1]http://www.safranmedialibrary.com/Photos/media

at the mesoscopic and microscopic scales [57, 58].

The goal of this work is to perform dual-scale steady fluid flow numerical simulations within 3D interlock woven fabric unit cells at the mesoscale in order to estimate their permeability tensor. This tensor is not necessarily aligned with the (X, Y, Z) global coordinate system of the unit cell when talking about anisotropic porous media as explained in [23]. Following this article guidelines, no assumption is made in the present work on the permeability tensor (orientation and symmetry). A numerical simulation approach allows in this case to predict the flow with a refinement level very challenging to achieve experimentally. The RTM process involves a preform compaction, and thus variations of both the inter-yarn domain morphology and the intra-yarn FVF. The main **objective** of this study is to decouple these variability factors, the mesoscopic unit cell morphology and the intra-yarn permeability field, and characterize their decoupled variations on the fabric permeability. **The textile model, intra-yarn permeability calculation, physical model, meshing procedure, numerical strategy and geometrical reduction of the present work are described in Section 2.** The characteristics of all the simulations performed in this work are presented in Section 3.1. The results of a mesh sensitivity study are shown in Section 3.2. The compaction and the geometrical reduction of the unit cell are then investigated in respectively Section 3.3 and Section 3.4, in addition to the changes within the intra-yarn FVF field in Section 3.5. The previous results are then confirmed in Section 3.6 by an analysis of the streamlines within the unit cells. All these results are finally discussed in Section 3.7 and conclusions are presented in Section 4.

2. Materials and methods

2.1. Textile model

The software Multifil, developed to solve a mechanical equilibrium of a medium composed of tangled beams, has been used for simulating the 3D angle-interlock woven fabric studied hereinafter. Note that these simulations have been performed at sub-mesoscale models which attempt to describe the behavior of the constitutive model from an elementary description of the constituting fibers, assuming that contact and friction are the main phenomena responsible for the (mesoscale) yarn behavior [59–61]. However, since the great number of carbon filaments in classical yarns (often several tens of thousands) is inaccessible, beams are seen such as "virtual" fibers, each grouping multiple actual fibers. Note that this software has implemented recently an enriched kinematical beam approach [62] to perform simulation directly at the mesoscale.

The woven pattern and the yarn features (*i.e.*, the number of carbon fibers per yarn, their mechanical properties and their twist) are input parameters with known values. The 3D woven fabric studied in this work is a ply-to-ply angle-interlock, composed of 27 carbon fiber yarns: 12 warp and 15 weft. All yarns are of the same type and size (48k). The weft yarns are distributed alternately in a sequence of 3 and 2 yarns in two consecutive columns. Concerning the warp, each column is composed of 2 yarns. In this sample, there are 6 warp planes and 6 weft columns.

In the end, the output unit cell is described by both the mesoscale yarn morphology and the intra-yarn FVF field which up-scales the microscopic intra-yarn morphology as shown in Figure 2. It is noteworthy that the textile modeling is periodic at the sub-mesoscale but the yarn envelope algorithm, devoted to recover the mesoscale, leads to a quasi-periodic numerical modeling. Besides, this textile is a unit pattern and so could be tesselated for building a greater textile. Moreover, the homogenization procedure has to rely on the concept of the Representative Volume Element (RVE) by respecting *(i)* a volume large enough to be statistically representative of a heterogeneous material and *(ii)* a constitutive response which is independent of the applied boundary conditions [63]. Therefore, in the subsequent, the domain, on which the effective permeability will be calculated, will be named Unit Cell (UC) or Representative Volume Element (RVE). However, contrary to the initial domain, the reduced ones, used for the sensitivity test on the inter-yarn porous space as detailed in Section 2.2.5, could not be referenced as a unit cell in theory since they are not periodic anymore but it is assumed that the homogenization procedure could still be performed for determining the effective permeability.

Finally, yarns are described by their neutral fibers (virtual curves going through mechanically homogeneous yarn sections centroids) along which consecutive cross sections are anchored to a master point of the yarn path. Thus, yarns could be seen as homogeneous porous media characterized by a permeability tensor. Moreover, it must be added that any Textile Geometry Pre-Processors (TGP) or Textile Generating Software (TGS) [34] can be used to generate the mesoscopic textile geometry. We denote by "as-woven" the non-compacted state of the fabric modeling and by "compacted" the one which is "as-manufactured" with respective unit cell dimensions of $18.9 \times 18.9 \times 4.9$ mm^3 and $18.9 \times 18.9 \times 2.4$ mm^3. In addition, the roving cross section average dimensions are 2×1 mm^2 for the as-woven unit cell and 2.5×0.5 mm^2 for the

compacted one. The unit cells corresponding to the as-woven and the compacted fabric are shown with their intra-yarn FVF fields in Figure 2.

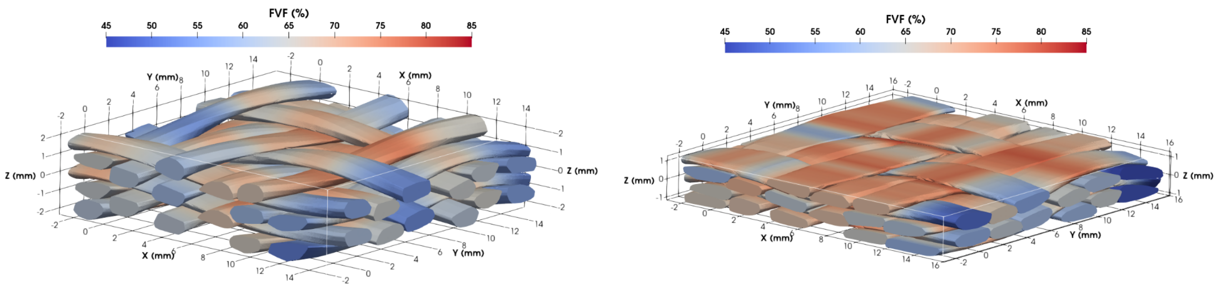

(a) (b)

Figure 2: **3D interlock unit cells with their intra-yarn FVF fields: (a) as-woven (29% global FVF) and (b) compacted (58% global FVF).**

2.2. *Methods*

2.2.1. *Intra-yarn permeability calculation*

The intra-yarn permeability tensor is assumed transversely isotropic and, as shown in Figure 3, is described by its eigenvalues K_I, K_{II} and K_{III} in its principal coordinate system $(\boldsymbol{e_I}, \boldsymbol{e_{II}}, \boldsymbol{e_{III}})$. Their numerical values are then calculated using the Gebart's law [64] shown in equation (1). **The mean value of the fiber radius R is 2.6 µm** and V_f the intra-yarn FVF value, $K_{III} = K_L$ corresponds to the longitudinal permeability and $K_I = K_{II} = K_T$ represent the transverse one. Both are determined accordingly to fiber orientation in a hexagonal arrangement

$$\begin{cases} K_T = \dfrac{16R^2}{9\pi\sqrt{6}} \left(\sqrt{\dfrac{\pi}{2\sqrt{3}V_f}} - 1 \right)^{\frac{5}{2}} \\ K_L = \dfrac{8R^2}{53} \dfrac{(1-V_f)^3}{V_f^2} \end{cases} \tag{1}$$

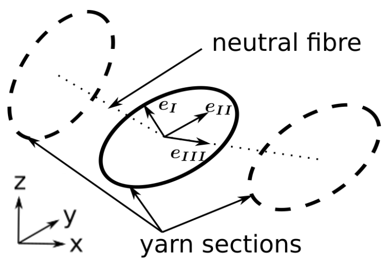

Figure 3: Coordinate system of a yarn section, with K_I, K_{II} and K_{III} its permeability components.

The intra-yarn **FVF and** permeability values computed in this way **for all the yarn sections** are presented in Figure 4 with their Probability Density Functions (PDF) for both as-woven and compacted unit cells. **The compaction appears to increase both intra-yarn FVF mean μ and standard deviation σ (see Figures 4a and 4b). Consequently, this leads to significantly lower both longitudinal and transverse intra-yarn permeability distributions means μ and to increase their standard deviations σ (see Figures 4c and 4d).**

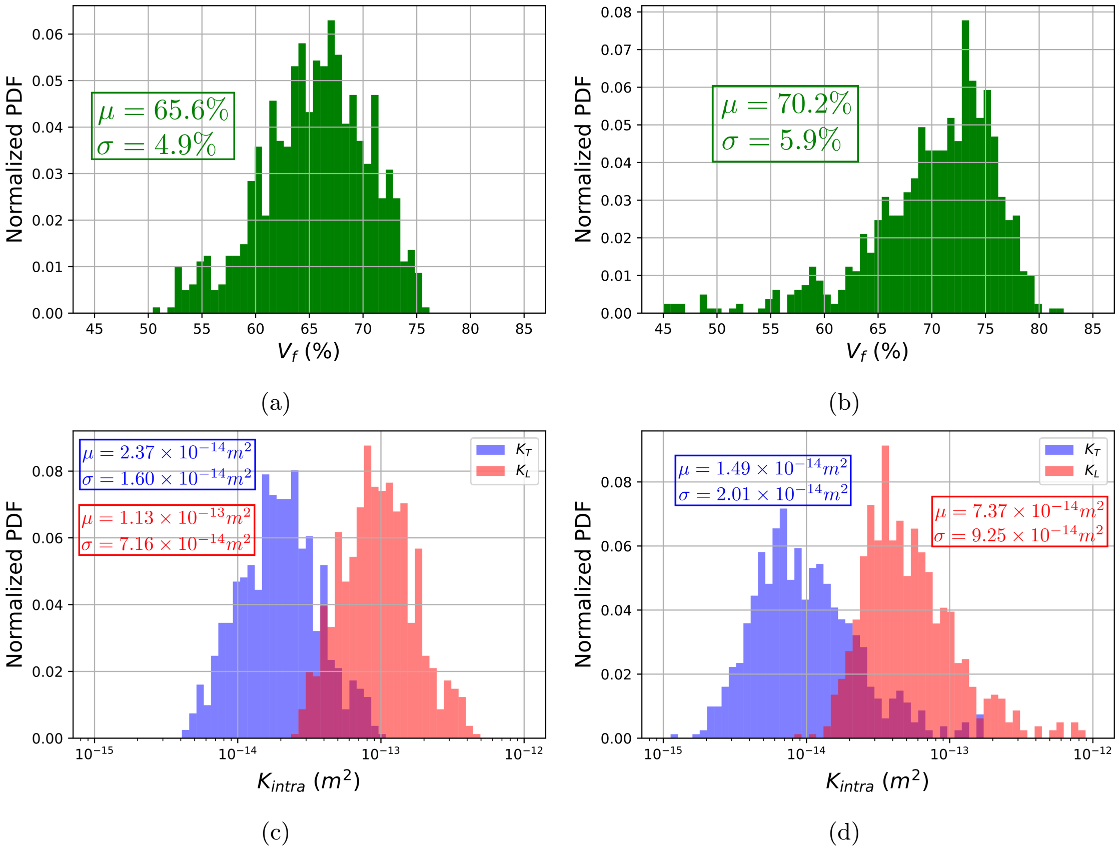

Figure 4: **Intra-yarn FVF and permeability Probability Density Functions (PDF) with their range of values: (a) - (c) as-woven ($K_T \in [4\times10^{-15}, 1\times10^{-13}]$ m^2 and $K_L \in [2\times10^{-14}, 5\times10^{-13}]$ m^2) and (b) - (d) compacted unit cells ($K_T \in [1 \times 10^{-15}, 2 \times 10^{-13}]$ m^2 and $K_L \in [9 \times 10^{-15}, 9 \times 10^{-13}]$ m^2).**

2.2.2. *Physical modeling*

The goal is to perform numerical simulations of the dual-scale fluid flow within the mesoscopic 3D interlock woven fabric unit cells at steady state in order to compute their permeability tensor. To do so, the following physical model has been built. The fluid flow is considered at steady-state because we aim to compute what is commonly referred to as the saturated permeability which only describes the geometrical drag [13], in opposition to the unsaturated permeability. The later does not only depend on the yarns morphology and material behaviors, but also on the fluid velocity and capillary effects [24, 65]. Moreover, the fluid flow is also considered laminar (*i.e.*, at small Reynolds number $Re \ll 1$) due to the low velocities (around 0.1 mm.s^{-1}) involved in the RTM process with resins such as epoxy [66, 67]. This hypothesis is confirmed *a posteriori* by computing the Reynolds number from both the mesoscale unit cell morphology and the velocity field. With the example of a flow along the X axis, the inter-yarn domain is modeled as an equivalent parallelepipedic volume with the same length L_X as the unit cell and a square cross-section of area L_c^2. L_c is the characteristic length used along with the characteristic velocity v_c, computed as the mean of the v_x velocity component over the unit cell, to compute Re in the X direction. The same method is applied to also get values of Re for flows along the Y and Z axis. The incompressible fluid flow between and within the yarns is modeled differently in order to account for its **dual-scale** feature. Let's denote by $\Omega \subset \mathbb{R}^3$ the unit cell domain made up by two non intersecting subdomains Ω_s (Stokes domain) and Ω_d (Darcy domain) separated by the interface $\Gamma = \partial\Omega_s \cap \partial\Omega_d$. Therefore, for a Newtonian fluid flowing in Stokes' domain between the yarns, the momentum and mass conservation equations lead to

$$\begin{cases} -\nabla \cdot \left(2\mu\dot{\boldsymbol{\varepsilon}}\left(\boldsymbol{v_s}\right)\right) + \nabla p_s = 0 \\ \nabla \cdot \boldsymbol{v_s} = 0 \end{cases} \text{in } \Omega_s \tag{2}$$

Similarly, for a Newtonian fluid flowing in and Darcy's domain within the yarns, the equations are defined such as

$$\begin{cases} -\mu\boldsymbol{K}_{\boldsymbol{intra}}^{-1} \cdot \boldsymbol{v_d} + \nabla p_d = 0 \\ \nabla \cdot \boldsymbol{v_d} = 0 \end{cases} \text{in } \Omega_d \tag{3}$$

The velocity-pressure pair is noted $(\boldsymbol{v_s}, p_s)$ in the Stokes domain Ω_s and $(\boldsymbol{v_d}, p_d)$ in the Darcy domain Ω_d. $\boldsymbol{K_{intra}}$ is the intra-yarn permeability tensor, $\mu = 0.2$ Pa.s the dynamic viscosity of the fluid modeled as Newtonian and $\dot{\boldsymbol{\varepsilon}}\left(\boldsymbol{v_s}\right) = \frac{1}{2}\left(\nabla\boldsymbol{v_s} + \left(\nabla\boldsymbol{v_s}\right)^T\right)$ the strain rate tensor.

We denote by $\Gamma_{s,D}$ and $\Gamma_{s,N}$ the non intersecting boundaries of Ω_s where respectively the Dirichlet and Neumann conditions are applied, and similarly $\Gamma_{d,D}$ and $\Gamma_{d,N}$ the non intersecting boundaries of Ω_d where respectively the Dirichlet and Neumann conditions are applied

$$\begin{cases} \boldsymbol{v_s} = \boldsymbol{v_0} & \text{on } \Gamma_{s,D} & \text{and} & \boldsymbol{\sigma} \cdot \boldsymbol{n_s} & = -p_{ext}\boldsymbol{n_s} & \text{on } \Gamma_{s,N} \\ \boldsymbol{v_d} \cdot \boldsymbol{n_d} = \boldsymbol{v_0} \cdot \boldsymbol{n_d} & \text{on } \Gamma_{d,D} & \text{and} & p_d & = -p_{ext} & \text{on } \Gamma_{d,N} \end{cases} \tag{4}$$

where $\boldsymbol{n_s}$ is the normal to $\partial\Omega_s$, $\boldsymbol{n_d}$ is the normal to $\partial\Omega_d$, $\boldsymbol{\sigma}$ the stress tensor, $\boldsymbol{v_0}$ the velocity and p_{ext} the pressure prescribed to the fluid. All the numerical simulations performed have a pressure drop ΔP applied between the inlet and outlet faces of our unit cells, while the null normal velocity condition $\boldsymbol{v} \cdot \boldsymbol{n} = 0$ is applied on their other faces. Moreover the continuity of the normal velocity and stress are the conditions applied at the interface Γ between both domains whose normal is $\boldsymbol{n_\Gamma} = \boldsymbol{n_s} = -\boldsymbol{n_d}$

$$\begin{cases} \boldsymbol{v_s} \cdot \boldsymbol{n_\Gamma} = \boldsymbol{v_d} \cdot \boldsymbol{n_\Gamma} & \text{on } \Gamma \quad \text{(Continuity of normal velocity)} \\ \boldsymbol{n_\Gamma} \cdot \boldsymbol{\sigma}\left(\boldsymbol{v_s}, p_s\right) \cdot \boldsymbol{n_\Gamma} = \boldsymbol{n_\Gamma} \cdot \boldsymbol{\sigma}\left(\boldsymbol{v_d}, p_d\right) \cdot \boldsymbol{n_\Gamma} & \text{on } \Gamma \quad \text{(Continuity of normal stress)} \\ 2\boldsymbol{n_\Gamma} \cdot \dot{\varepsilon}\left(\boldsymbol{v_s}\right) \cdot \boldsymbol{\tau_\Gamma} = -\dfrac{\alpha}{\sqrt{\boldsymbol{\tau_\Gamma} \cdot \boldsymbol{K_{intra}} \cdot \boldsymbol{\tau_\Gamma}}} \boldsymbol{v_s} \cdot \boldsymbol{\tau_\Gamma} & \text{on } \Gamma \quad \text{(BJS condition)} \end{cases} \tag{5}$$

The Beavers-Joseph-Saffman (BJS) condition is also considered [68] to link the tangential fluid velocity on Γ to its shear rate through the porous medium permeability and a numerical coefficient $\alpha = 1$ in this work. **Considering the very low permeability values in the yarns and the numerical methods implemented in this study for the Stokes-Darcy coupling, the value of this coefficient has no significant influence on the flow [55].** Because the present work stands in a 3D space, the tangential vector to the interface $\boldsymbol{\tau_\Gamma}$ is defined by projection of the velocity vector onto the interface Γ. The whole physical model is synthesised within the Figure 5.

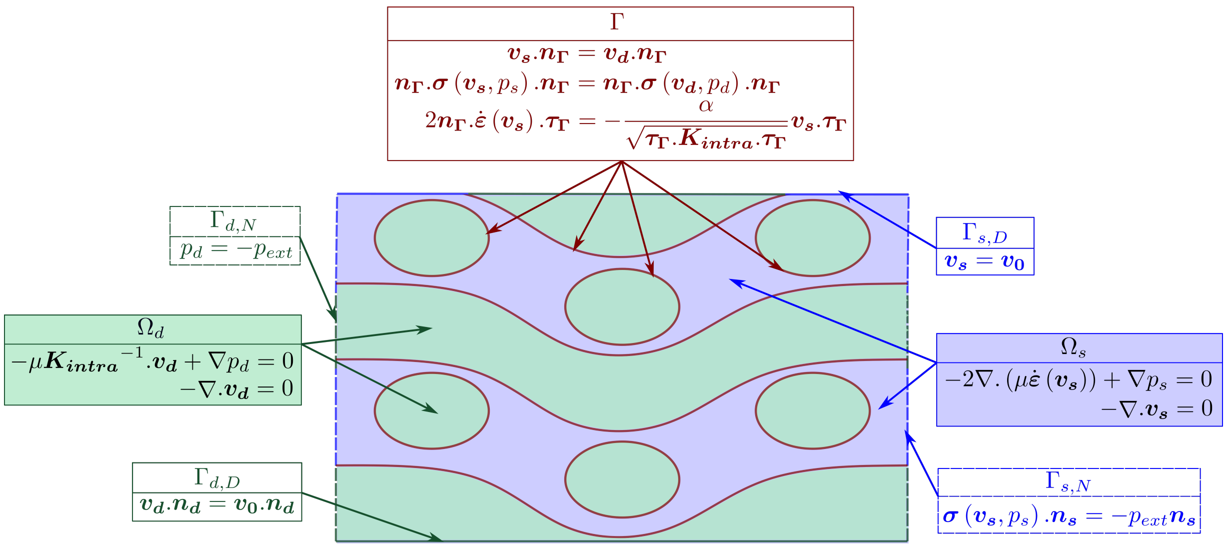

Figure 5: **Summary of the physical modeling of the double-scale Stokes-Darcy coupled fluid flow within a woven fabric.**

2.2.3. Meshing procedure

An unstructured tetrahedral mesh is used because it is more efficient to mesh the complex 3D interlock yarns and because it is required when using a stabilized $P1/P1$ formulation [54–56]. Moreover, the way the meshing procedure is performed allows the mesh to be conformal. This means that the interface between the inter-yarn and intra-yarn domains is directly described by the mesh nodes, since elements from both parts of the interface have matching nodes on it as shown in Figure 6.

The method used for meshing both textile and resin areas is composed of two main steps: *(i)* the whole domain is firstly meshed with voxels by REVoxel software [69] and *(ii)* this voxel mesh is then remeshed with tetrahedra by Mirax software after a smoothing operation on the quadrangle surface mesh of the yarns. The latter is used in order to remove the jagged effect of the voxel representation. This smoothing is performed by a constrained Catmull-Clark procedure associated with a control of the yarn volume.

Note that, similarly to the textile geometry modeling, other meshers allowing to perform directly a tetrahedral mesh could actually also be used. The result of these two steps is shown in Figure 7 for both yarns and inter-yarn spaces. Note that the initial voxel mesh is performed at a resolution from 70 to 100 µm. The initial 100 µm voxel mesh of the as-woven unit cell has about 10 million voxels and the compacted one about 5 million voxels. At the end, the as-woven unit cell has about 12 million tetrahedra and 2 million nodes and the compacted one about 7 million tetrahedra and 1 million nodes.

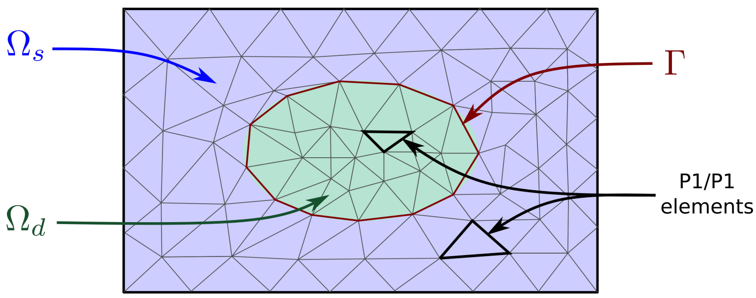

Figure 6: Monolithic approach of the Stokes-Darcy coupled problem with its unstructured mesh and its conformal interface **(the mesh is drawn here just for illustrative purposes)**.

2.2.4. Numerical strategy

The numerical strategy used in this work is based on a mixed velocity-pressure finite element formulation implemented within the Z-set software [70]. The monolithic approach of the Stokes-Darcy coupled problem

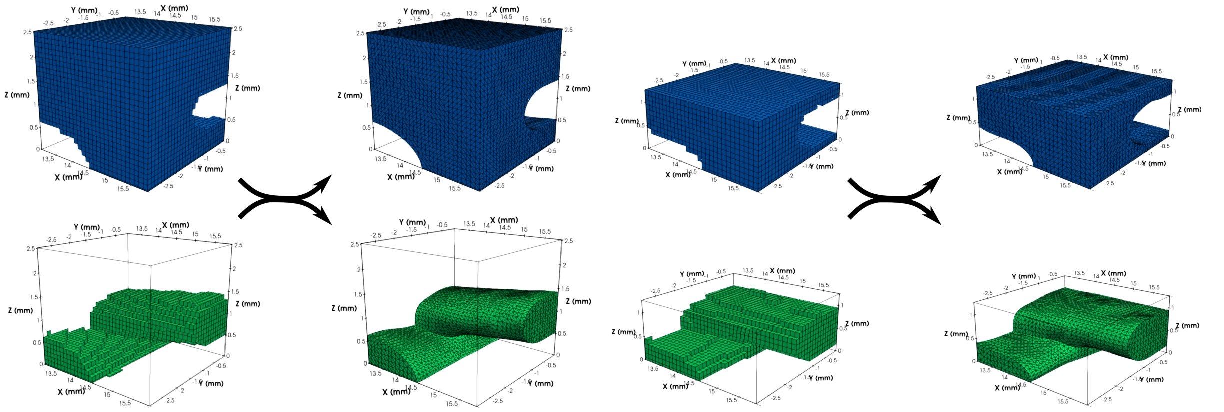

(a) (b)

Figure 7: **Corner of the 3D interlock unit cell meshed with 100 µm voxels (left) and then with tetrahedra (right): (a) as-woven unit cell and (b) compacted unit cell, where the upper row represents the inter-yarn domain and the bottom row the yarns.**

illustrated in Figure 6 is characterized by a single mesh for both domains modeled by Stokes and Darcy equations. In this work, the same approximation order is chosen for both velocity and pressure fields. Piecewise linear approximation are here considered for both fields. Such a $P1/P1$ formulation is not stable, so a **Variational MultiScale** (VMS) method is introduced to stabilize it. The idea of the VMS framework is to decompose the space of the unknown into the finite-dimensional space and an infinite-dimensional one, improving the stability of Galerkin finite element method [54]. The main task behind the method is to model the infinite scale or subscales in terms of the resolved finite element scales. This yields two problems: a finite element scale problem and a subgrid problem. In the Algebraic SubGrid Scale (ASGS) method [54], the subgrid fields are directly proportional to the finite element residuals. The detailed stabilized weak formulation can be found in [55].

The effective permeability tensor $\boldsymbol{K_{eff}}$ of the unit cell is finally computed from velocity and pressure fields of three numerical simulations, corresponding to the X, Y and Z directions of the main flow, through the Darcy's law as follows

$$\boldsymbol{v} = -\frac{1}{\mu}\boldsymbol{K_{eff}} \cdot \boldsymbol{\nabla p} \tag{6}$$

Because no assumption are made on this tensor, and by using the 3D-generalised Darcy's law (equation (6)), all its nine components are computed. The permeability tensor $\boldsymbol{K_{eff}}$ is then diagonalized to analyze its eigenvectors and eigenvalues.

2.2.5. *Unit cell reduction*

The racetracking phenomenon needs a particular attention when attempting to assess the permeability tensor of a textile media. Usually, they are located near the unit cell boundaries as experimentally observed by a faster flow front between the textile and the mold [71]. Furthermore, some works have proven its non-negligible effect on the fabric permeability characterization [16], leading to a global overestimation of the latter.

Figure 8 and Figure 9 show the initial unit cell and two domains coming from its reductions where their in-plane dimensions are cut of 10% and 20%. It is especially noticeable, on the woven top-view Figure 9, that the reduction erases the preferential flow channels near the unit cell boundaries, due to the residual yarn overlengths, set for allowing the crimp during the woven textile modeling. So, these in-plane reductions are targeted to remove the undesirable areas of preferential flows through the thickness as well as in the woven cross section in weft and warp directions. It should be precised that, whereas the whole domain can be assimilated as a unit cell, the reduced domains could not since they are not periodic anymore.

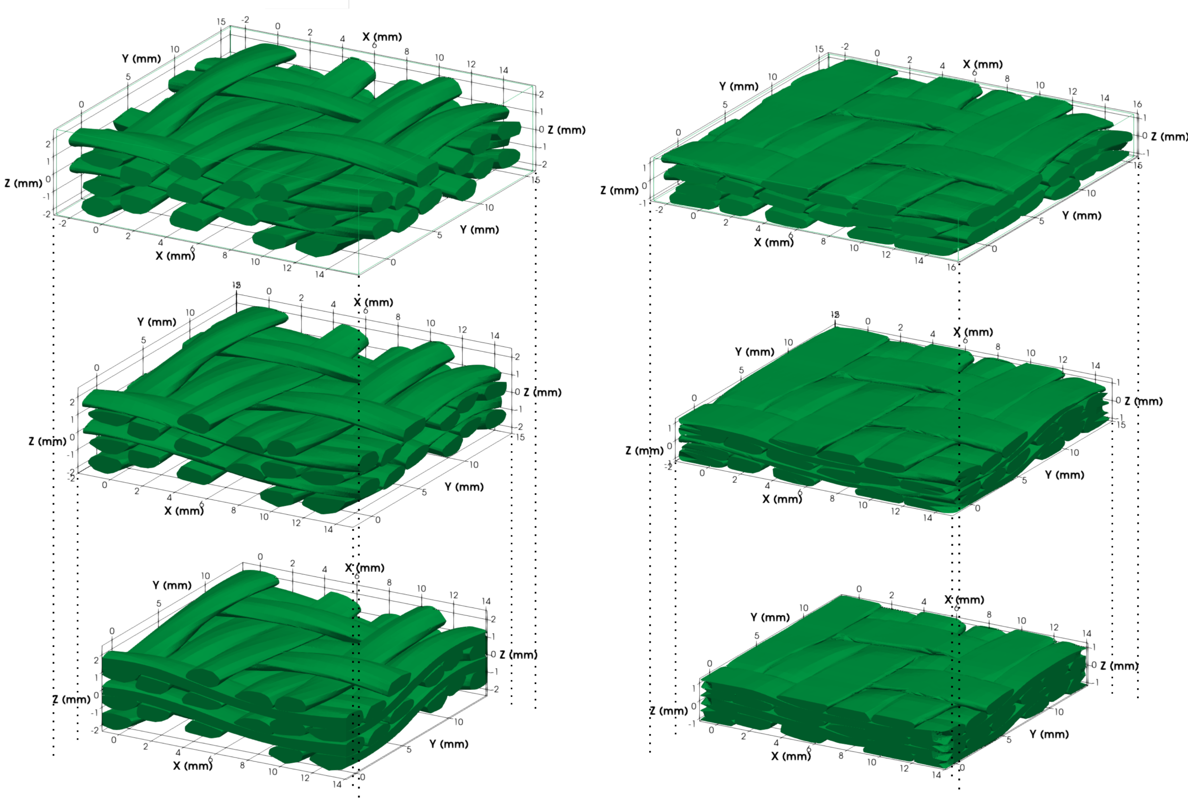

(a) (b)

Figure 8: **(a) As-woven and (b) compacted unit cells reduced by 0%, 10% and 20% on the (X,Y) plane.**

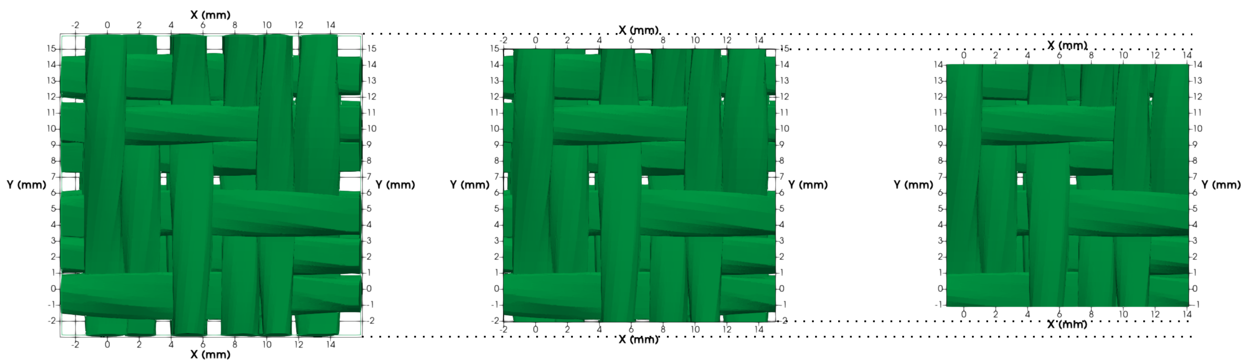

Figure 9: **Top view of an as-woven unit cell reduced by 0%, 10% and 20% on the (X,Y) plane.**

3. Results

Several parameters accounting for whether the fabric mesoscopic morphology, the intra-yarn FVF field or the unit cell mesh element size are set to vary in the results presented hereafter. They can thus have an impact on the fabric permeability tensor $\boldsymbol{K_{eff}}$, what has been investigated. Firstly, a mesh sensitivity study has been performed on the as-woven unit cell. The comparison between the as-woven and compacted unit cells will then show the effect of the fabric compaction on $\boldsymbol{K_{eff}}$. Because preferential flow channels are observed near the unit cell boundaries, a geometrical reduction of its size is performed and its consequences on $\boldsymbol{K_{eff}}$ is thus studied. Finally, variations in the intra-yarn FVF field leading thus to variations in the intra-yarn permeability field can also change $\boldsymbol{K_{eff}}$ values.

3.1. Numerical performances

Numerical simulations performed for this work were solved with the direct solver **MUMPS (MUltifrontal Massively Parallel Solver) [72]** in distributed mode on 10 to 20 cluster nodes on two different clusters. **For the parallelism, MUMPS solver distributes the work tasks among the processors by partitioning the mesh into sub-domains.** The first one(a) involves nodes with 2 Intel Xeon Gold 6132 CPU with 14 cores at a frequency of 2.6 GHz and 128 Go of RAM, and the second one(b) nodes with Intel Xeon Gold 6342 (Intel Ice Lake generation) CPU with 2×24 cores at a frequency of 2.8 GHz and 263 Go of RAM. **The number of degrees of freedom in velocity and pressure (DOF), nodes per sub-domains, computation time and also the memory used are particularly reported in Table 1 for each model. For this numerical model, the direct solver MUMPS gives an increase of the memory used along with the number of DOF.**

3.2. Mesh sensitivity study

The as-woven unit cell is meshed with four different voxel sizes: 70, 80, 90, and 100 µm. The aim is to check if the mesh is sufficiently refined to ensure a consistent value of the unit cell permeability tensor. **Note that voxel meshes are just intermediates in the meshing process, the simulations are all done on tetrahedral meshes.** The results shown in Figure 10 do not present a clear variation of the permeability components even if a small decrease can be observed when refining the mesh. **It is found that the relative differences between the 70 and 100 µm voxel size is about 5% for K_{xx} and K_{yy} components, and 8% for K_{zz} component, when looking at the full unit cell. The same results are found for in-plane component permeability on the 10% and 20% reduction of the domain**

Unit Cell (UC)	Global FVF (%)	Voxel size (µm)	UC Reduction (%)	Nb of DOF ($\times 10^6$)	Nb computational nodes / sub-domains	Execution Time (h)	Memory used (Go)
As-woven	29	100	0	8.3	10 / 10	6.1[a]	NA
			10	7.0	10 / 10	2.9[a]	460
			20	5.5	10 / 10	1.9[a]	355
		90	0	11.0	10 / 10	9.6[a]	610
			10	9.1	10 / 10	6.2[a]	570
			20	7.2	10 / 10	3.4[a]	480
		80	0	15.0	15 / 15	10.7[a]	970
			10	12.5	15 / 15	6.7[a]	950
			20	9.9	15 / 15	4.6[a]	760
		70	0	21.5	13 / 26	0.4[b]	460
			10	19.2	20 / 20	13.3[a]	1390
			20	14.5	15 / 15	11.5[a]	1000
Compacted	58	80	0	8.8	8 / 8	1.6[a]	400
			10	7.1	8 / 8	1.2[a]	320
			20	5.7	8 / 8	1.1[a]	260
		70	0	12.7	10 / 10	5.9[a]	600
			10	10.4	10 / 10	4.1[a]	560
			20	8.3	10 / 10	4.2[a]	460

Table 1: **Simulation data (the column “Nb of DOF” refers to the number of degrees of freedom in the tetrahedral mesh).**

between the 70 and 100 µm voxel size, whereas K_{zz} appears to increase its relative differences up to 27%. Therefore, it confirms that K_{xx} and K_{yy} are not really sensitive to the initial voxel size (in the studied range, *i.e.*, between 70 and 100 µm), whereas K_{zz} remains so.

3.3. Effect of the fabric compaction on its permeability

The first variation of the mesoscale morphology is studied through the compaction of the fabric. To do so, both as-woven and compacted **full** unit cells, respectively 29% and 58% global FVF (with yarns considered as porous media), meshed with 80 µm voxels are compared. Fabric permeability tensors are analyzed also through their eigenvectors and eigenvalues, instead of just the diagonal components, since there is no specific assumption made on the tensors. Their diagonal components K_{xx}, K_{yy} and K_{zz} are the ones of first interest because the weaving pattern is built along the X, Y and Z axis. Moreover, the eigenvectors and eigenvalues of these tensors are computed.

Figure 11 shows the images of the unit sphere through the permeability tensor, normalizing by the highest

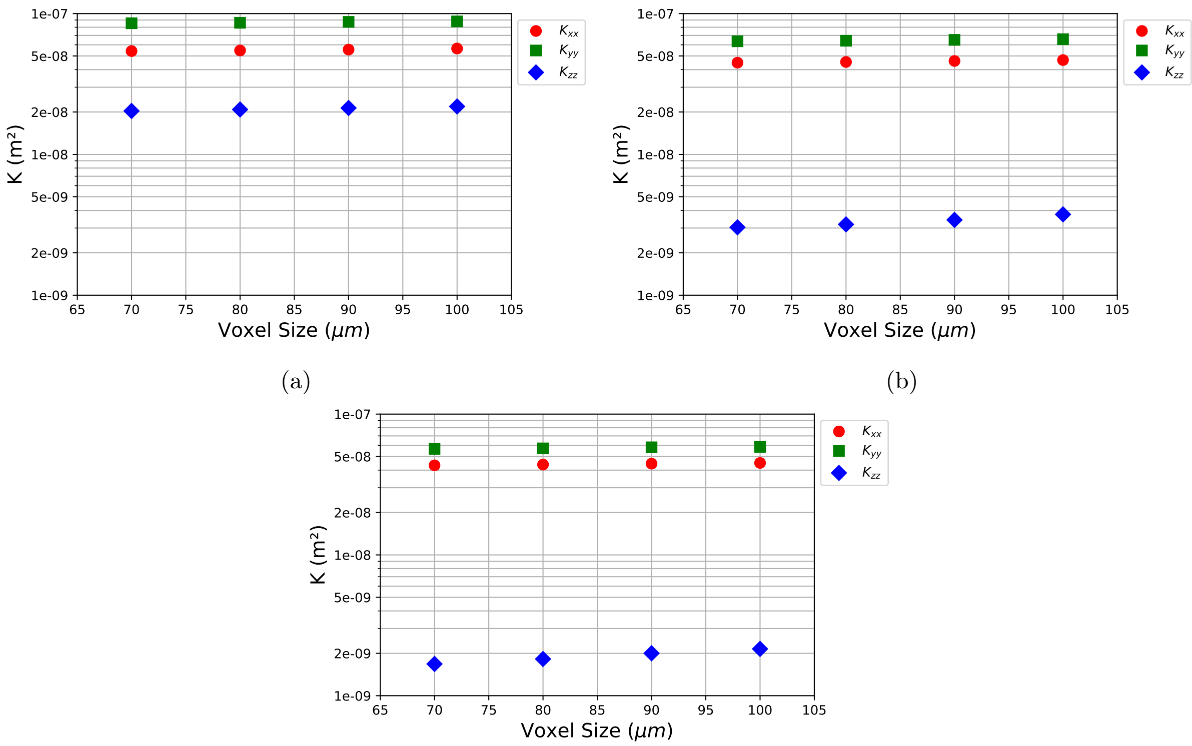

(a) (b) (c)

Figure 10: **Diagonal terms of the permeability tensor for as-woven unit cells meshed with different voxel sizes: (a) full unit cell, (b) 10% and (c) 20% reduced domains.**

eigenvalue. The eigenvectors allow to compare the orientation of the permeability principal coordinate system with the weaving pattern global coordinate system, and the eigenvalues allow to consider the permeability tensor anisotropy. By looking at the diagonal component K_{xx}, K_{yy} and K_{zz} of the permeability tensor on Figure 12, their values appear to be reduced by approximately 2 orders of magnitude through the unit cell compaction. **Moreover, the permeability tensor anisotropy is completely changed, since $\frac{K_{xx}}{K_{zz}} = 2.63$ for the as-woven unit cell and $\frac{K_{xx}}{K_{zz}} = 0.34$ for the compacted one.** The depictions of these permeability tensors shown in Figure 11 corroborate this observation.

Indeed the as-woven unit cell has the principal directions of its permeability tensor almost aligned with the global coordinate system, whereas the compacted unit cell shows a complete misalignment within the (X, Y) plane. The depiction of the compacted unit cell permeability tensor seen in Figure 11 is as such completely different from the as-woven one. This may be explained by the preferential flow channels (explained in Section 3.4) non-homogeneous distribution near the compacted unit cell boundaries. The wider channels being oriented along the Z axis, K_{zz} is thus unusually greater than K_{xx}. Moreover these

301 preferential flow channels have a greater effect on the compacted unit cell permeability than on the as-woven one. This occurs because the preferential flow channels close to the unit cell boundaries do not shrink under compaction, in opposition to the inter-yarn flow channels within the weaving pattern. Therefore, this non-homogeneous preferential flow channels distribution can also explain the observed in-plane misalignment of the permeability tensor.

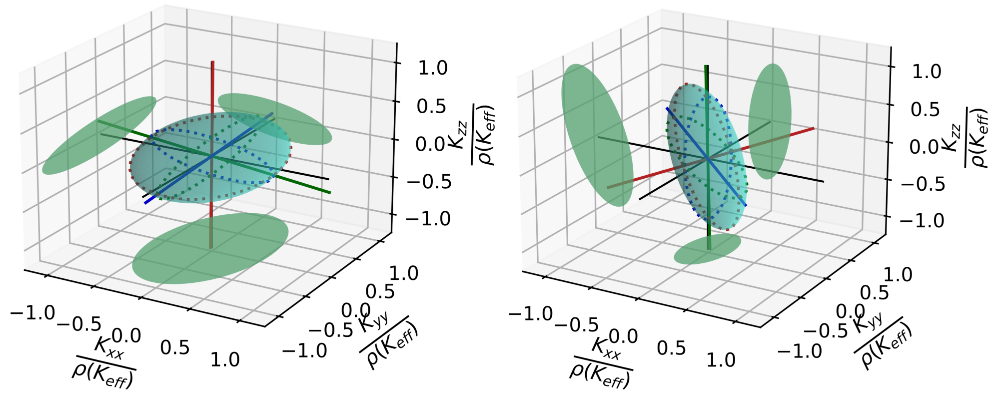

(a) (b)

Figure 11: **Image of the unit sphere through the permeability tensor $\boldsymbol{K_{eff}}$ normalised by its spectral radius $\rho(\boldsymbol{K_{eff}})$ of the (a) as-woven and (b) compacted full unit cells, colored lines representing its principal coordinate system.**

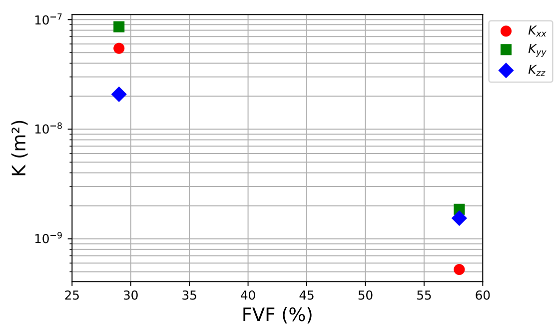

Figure 12: Diagonal terms of the permeability tensor for both unit cells.

306 *3.4. Effect of the unit cell reduction on its permeability*

307 **As discussed in section 2.2.5, in-plane geometrical reductions of 10 % and 20 % have been applied on both as-woven and compacted unit cells. The aim is to avoid as much as possible the side effects from racetracking phenomenon while respecting the representativeness of the textile and hence to show the effect of this reduction on the effective permeability. Note that the results of this sensitive study are stemming from an initial voxel mesh of 80 µm.**

By looking closely the velocity field on the top side of the domain (see Figure 13), one can acknowledge the existence of preferential flow channels characterized by higher velocities compared to those within the domain. They are located near boundaries, similarly to those experimentally observed, underling hence the aforementioned racetracking phenomenon. This confirms that, in our case, the fluid flows partly outside the weaving pattern, leading thus to an overestimation of the fabric permeability and the need for reducing the computed domain.

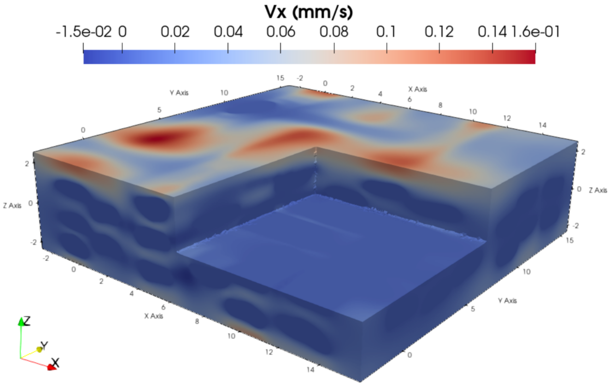

Figure 13: Flow along the X direction in the as-woven unit cell, v_x component of the velocity field.

Figure 14 shows the evolution of the diagonal components of $\boldsymbol{K_{eff}}$ along with the unit cell reduction for both as-woven and compacted states. The results show first that all permeability component values strongly decrease between the initial and the 10% reduced unit cells. Between 10% and 20% unit cell reduction, the in-plane components, K_{xx} and K_{yy}, remain almost constant for both as-woven and as-manufactured states, by taking into account the related incertitudes, whereas the out-of-plane component, K_{zz}, still strongly decreases for both unit cells. The relative decrease of permeability tensor diagonal component from 0% to 10%, and 10% to 20% geometrical reduction are shown in Table 2. Indeed, this is mainly due to the discrepancies between the in-plane sections of the textile as shown previously in Figure 9.

Although these results are not sufficient to state the convergence of K_{zz} while reducing the unit cell, they prove that a 10% geometrical reduction of the unit cell boundaries is enough to avoid most of in-plane preferential flows. Thus, this method allows to get a more accurate value of these unit cell permeability tensor which is mainly related to its mesoscale morphology.

An analysis of the inter-yarn porosities over slices along the X and Y directions, respectively ϕ_X and ϕ_Y and computed as the ratio between the yarn area and the total slice area is therefore

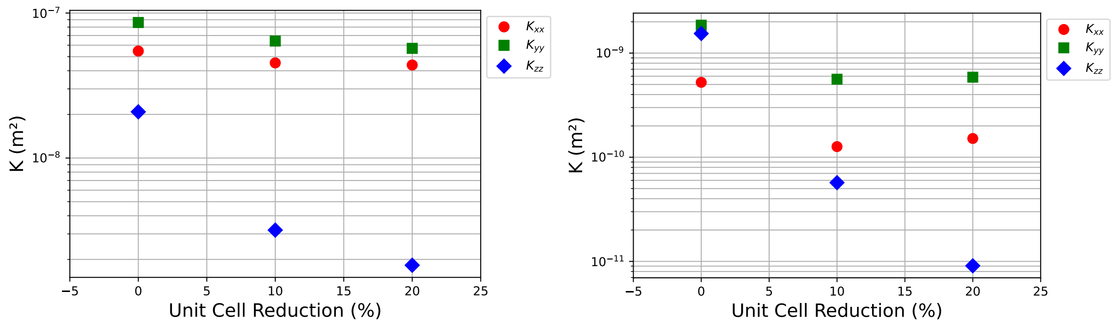

(a) (b)

Figure 14: Diagonal terms of the (a) as-woven and (b) compacted unit cell permeability tensors with their geometrical reduction.

Unit Cell (UC)	**Global FVF** (%)	**Permeability component**	**Rel. Decrease from** 0% **to** 10% **Geom. Red.** (%)	**Rel. Decrease from** 10% **to** 20% **Geom. Red.** (%)
As-woven	29	K_{xx}	17.2	3.3
		K_{yy}	25.5	11.0
		K_{zz}	84.7	42.8
Compacted	58	K_{xx}	75.9	-19.6
		K_{yy}	69.7	-4.6
		K_{zz}	96.3	84.1

Table 2: **Relative decrease of permeability tensor diagonal component due to geometrical reduction (a negative value means that the permeability component increases).**

carried on. Figure 15 shows the evolution of ϕ_X and ϕ_Y along the non-dimensional abscissa $a = \frac{x}{L_X}$ for ϕ_X and $a = \frac{y}{L_Y}$ for ϕ_Y. A common point with the previous permeability values is observed: a strong decrease when going from the boundary to the unit cell center. This point is consistent with the previous conclusion. Moreover, the permeability is known to vary alongside with porosity, and thus it can be hypothesised that the unit cell permeability follows **the same variations than ϕ. The oscillations between maximum and minimum porosity values observed far from the unit cell boundaries can be explained by the location of the warp and weft yarn columns. In the end, defining, and so predicting, the actual value of the unit cell permeability is a complex task, since the inter-yarn porosity is strongly heterogeneous, even if it is periodic.** It may be interesting to give a range in which the permeability values of the mesoscopic unit cell lie, in addition to its mean value. Such detailed permeability computing can be achieved through the investigation of more unit cell reduction percentages that will be carried out in further works.

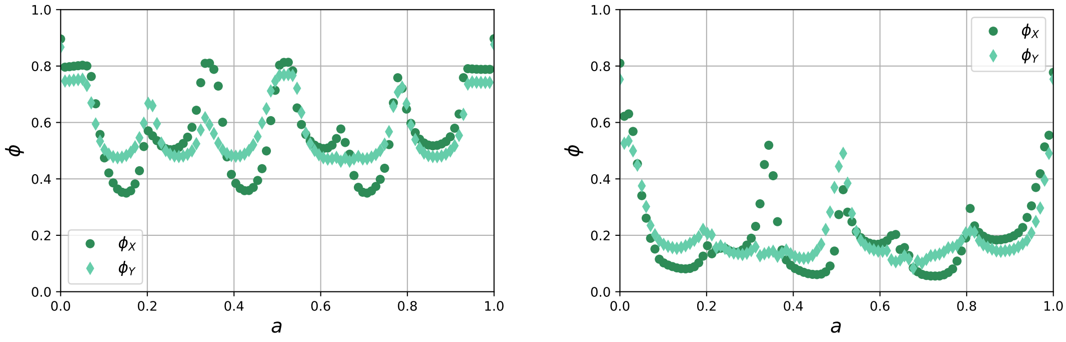

(a) (b)

Figure 15: Inter-yarn porosities ϕ_X and ϕ_Y of slices along respectively the X and Y directions of the (a) as-woven and (b) compacted unit cell.

3.5. Effect of intra-yarn permeability variations on the fabric one

The high fidelity modeling of the fabric unit cell provides accurate information on the 3D woven such as the intra-yarn FVF field at level of yarn cross sections. This means that a different value of intra-yarn FVF could be used to characterize each yarn section, and likewise with intra-yarn permeability tensors which are computed directly from intra-yarn FVF values. The aim is to investigate how much the settings linked to the intra-yarn permeability field changes the fabric permeability according to the level of definition. Three intra-yarn permeability levels of definition shown in Figure 16 are compared. The first level is the most discretized level by setting the intra-yarn permeability field. **The second level is an intra-yarn permeability averaged for each yarn and the third level is an intra-yarn permeability averaged over all the yarns.** The relative difference between the fabric permeability tensors with regards to an intra-yarn permeability field defined per yarn section $\boldsymbol{K_{section}}$ is computed by:

$$\frac{||\boldsymbol{K_i} - \boldsymbol{K_{section}}||_{2,2}}{||\boldsymbol{K_{section}}||_{2,2}} \quad \text{with} \quad i \in \{yarn, global\} \tag{7}$$

where $\boldsymbol{K_{yarn}}$ and $\boldsymbol{K_{global}}$ are the fabric permeability tensors computed from one permeability tensor per respectively yarn and for all the yarns, by using the spectral norm defined by:

$$||\boldsymbol{K}||_{2,2} = \underset{||\boldsymbol{x}||_2 \leq 1}{sup} ||\boldsymbol{Kx}||_2 = \sqrt{\rho\left({}^t\boldsymbol{KK}\right)} \tag{8}$$

where ρ is the tensor spectral radius.

The results for both 10% and 20% reduced unit cells, meshed with 80 µm voxels, are presented in Figure 17

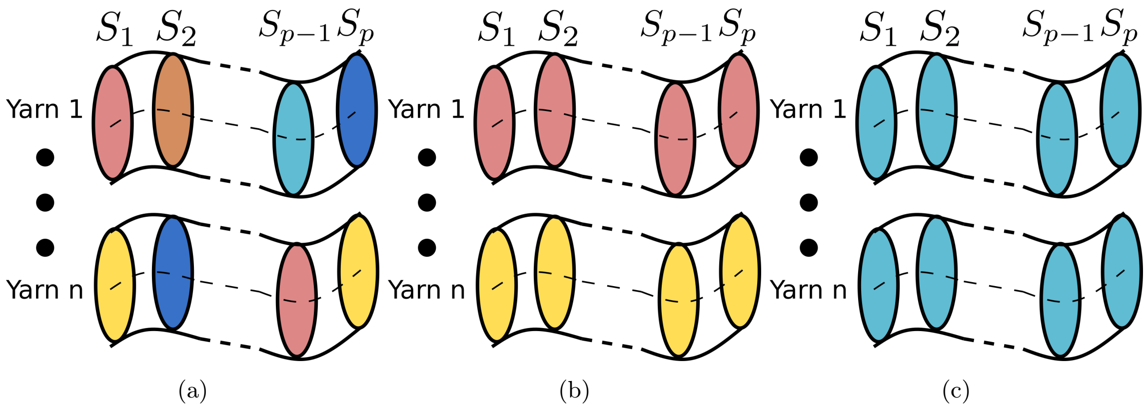

Figure 16: Intra-yarn permeability field levels of definition: (a) section, (b) yarn and (c) global.

where no significant difference can be seen on K_{xx}, K_{yy} and K_{zz} between the different intra-yarn permeability levels of definition. Relative differences were computed to investigate the potential differences on the whole tensors, all of them are smaller than 1%. Then, there is no significant effect of the intra-yarn permeability field variability on these unit cell permeability at steady state. A first explanation could be the very low intra-yarn permeabilities compared to the inter-yarn flow channel width. As a consequence, the fabric permeability would be more affected by its mesoscale morphology than by the intra-yarn flow. As such, the variations of local intra-yarn permeability have a weak impact on the flow within the whole unit cell, and hence on the fabric permeability. Moreover, it can be thought that different laws linking the intra-yarn FVF to the intra-yarn permeability such as in [28, 31, 73] will lead to the same results, *i.e.*, relative differences between permeability tensors smaller than 1%. This could therefore confirm the non significant effect of intra-yarn permeability variability on the saturated permeability of these unit cells. **These conclusions may lead to think that a single-scale flow simulation is enough to compute numerically the effective permeability of these unit cells. However, the inter-yarn domain of the compacted unit cell may not percolate from the inlet to the outlet boundary. As a consequence, a finite element resolution of the Stokes flow only in a non-percolating domain is impossible and thus the resolution of the Stokes-Darcy flow is mandatory.**

3.6. Assessment of the balance between inter- and intra-yarn flows

The fluid flows at a double-scale level, both between and within the yarns. Streamlines are observed in Figure 18 to determine where most of the fluid goes through. This allows to figure out the relative weight of inter- and intra-yarn characteristics on the overall flow within the fabric, and thus on the prediction of the permeability.

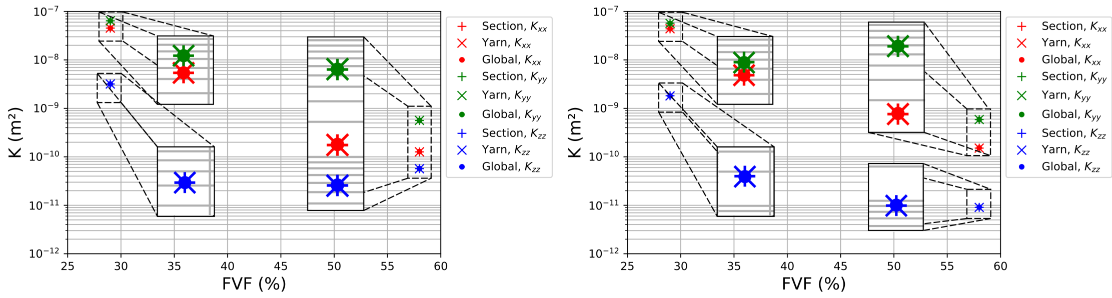

(a) (b)

Figure 17: Diagonal terms of the permeability tensor for (a) 10 % and (b) 20 % reduced unit cells **(a zoom is made to clearly show that the points are superposed)**.

This analysis shows that the fluid flows mainly around the yarns, with only small velocities involved within them. This is due to the very low values of intra-yarn permeabilities compared to the inter-yarn flow channel width. Thus, the fabric permeability is as a consequence mainly determined by its mesoscale morphology, rather than by its intra-yarn permeability field. This confirms the previous results shown through this work, especially **that the fabric compaction has a much greater effect on the fabric permeability than the local intra-yarn permeability field variations**.

The laminar flow hypothesis is now verified by computing the Reynolds number from both the mesoscale unit cell morphology and the velocity field. L_c ranges between 2 and 14 mm and v_c between the orders of 10^{-4} and 10^{-1} mm.s^{-1} for the simulations performed in this work. The resulting Re values are between the orders of 10^{-6} and 10^{-2}, thus confirming the laminar flow hypothesis.

3.7. Discussion

Considering the results presented above, some statements can be made on saturated fluid flow simulations at the mesoscopic scale, while other points may benefit from additional investigations that will brighten the associated results. Firstly, it can be set that the initial voxel mesh size of our unit cells should be **equal to or smaller than** 100 µm. This is highly related to the yarns mesoscopic morphology, but most of all to the width of the channels between them that can be very small. As a consequence, a high resolution mesh is mandatory to precisely solve the numerical flow problem within these areas. In addition, a 100 µm mesh size seems to be enough with regards to the in-plane components K_{xx} and K_{yy} of $\boldsymbol{K_{eff}}$. However, farther investigations may help to determine a mesh size below which the out-of-plane component K_{zz} will converge in the same way that the in-plane ones.

Qualitative observations of the streamlines within the fabric unit cells showed the fluid flowing mainly around the yarns rather than within them. This point seems to indicate that $\boldsymbol{K_{eff}}$ would be mainly determined by its unit cell mesoscopic morphology, and that variations in the intra-yarn characteristics would not change it so much. This statement was confirmed quantitatively by analyzes on both previous factors of variability of $\boldsymbol{K_{eff}}$.

A major point results from the preferential flow channels close to the unit cell boundaries. Being "outside" the weaving pattern core but still within the computational domain, the high velocities within these areas were found to lead to an overestimation of $\boldsymbol{K_{eff}}$. A geometrical reduction of the unit cells has thus been investigated to prevent it. It appeared clearly that a 10 % reduction is at least required to avoid most of in-plane preferential edge flows. Furthermore, it is enough for the converge of the in-plane components K_{xx} and K_{yy}, which is not the case for the out-of-plane component K_{zz}. The hypothesis of $\boldsymbol{K_{eff}}$ varying alongside porosity between a minimum and a maximum value within the weaving pattern core arises then. Not enough flow simulations on more unit cell reduction percentages have been performed until now to confirm this assumption. However, if this will be confirmed in future works, there will be a way by examining several reduction percentages to give an interval of permeability values for $\boldsymbol{K_{eff}}$ in addition to its mean value. Moreover, reduction of 30 % of the unit cells will be performed to see if the out-of-plane component K_{zz} converges. However, this may raise the question of the unit cell representativeness with regards to the weaving pattern. The second major point lies in the first importance the fabric compaction has in $\boldsymbol{K_{eff}}$ value, since two orders of magnitude are observed between the as-woven and compacted unit cells permeability values K_{xx}, K_{yy} and K_{zz}. Moreover, this huge effect of the fabric compaction is also visible on the permeability tensor anisotropy, as the compacted unit cell permeability tensor is misaligned in the (X, Y) plane. It may be assumed that a non-homogeneous distribution of the preferential flow channels in the X, Y and Z directions leads to this unusual result. Such hypothesis could be confirmed if the reduced compacted unit cells, with much less preferential flow channels, show a permeability tensor whose eigenvectors are aligned with the global coordinate system of the weaving pattern.

The last result about the effect of variations of the intra-yarn FVF field level of definition on $\boldsymbol{K_{eff}}$ confirms the previous qualitative observation on the streamlines. Relative differences between $\boldsymbol{K_{eff}}$ computed from an intra-yarn FVF field with a different value per yarn section and $\boldsymbol{K_{eff}}$ computed with others levels of definition are smaller than 1 %. Because the resulting intra-yarn permeability values are so low compared to the inter-yarn channel width, variability in the former field is not significant on these unit cells during the steady state. However, this result is related to Gebart's law, and using other laws to compute the intra-yarn permeability field would be interesting to confirm such an interpretation.

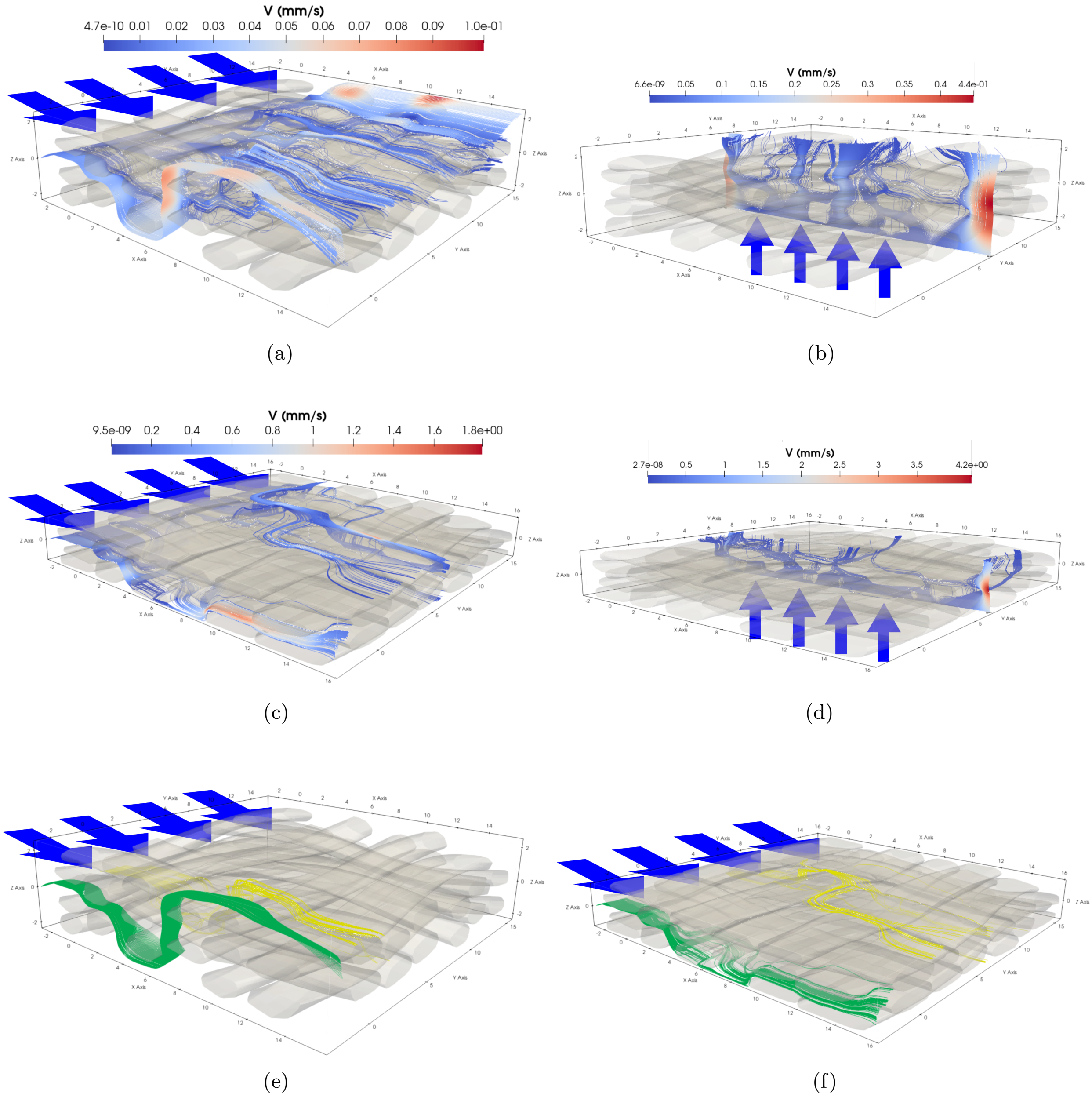

Figure 18: **Streamlines from the inlet boundary (defined by the blue arrows) for (a) - (b) as-woven and (c) - (d) compacted unit cells meshed at 80 μm voxels, with some of them going between yarns (green) and within yarns (yellow) in respectively (e) as-woven and (f) compacted unit cells.**

4. Conclusions and perspectives

A new method was proposed which can handle dual-scale flow simulations within complex mesoscale geometries of 3D woven textile, hence dertermining their effective permeability. A monolithic approach of a mixed velocity-pressure finite element formulation stabilized by a VMS method and implemented in the Z-set software is used to solve the Stokes-Darcy coupled problem.

The results shown that, in the assumption of a saturated flow, the intra-yarn permeability field, in the studied range, has a weak effect on the fabric permeability while the latter is mainly determined by the mesoscale morphology. However, we would like to our model be as complete as possible with taken into account intra-yarn realistic details such as permeability even if this parameter remains negligible among others.

Indeed, when studing different compaction levels of the woven fabric, it has been shown that this first kind of mesoscale morphology variation has the greatest impact on the permeability values. As such, the compacted fabric (58% global FVF) has permeability values of two orders of magnitude lower than the as-woven one (29% global FVF). It reveals that the relatively low intra-yarn permeability compared to the inter-yarn flow channel width is obviously responsible for a predominant inter-yarn flow. Moreover, the compaction leads to an orientation change in the unit cell permeability tensor, that can be a consequence of modification of the edge preferential flow channels.

The second kind of studied mesoscale morphology variation is the geometrical reduction of unit cells. It has been shown that preferential flow channels can be mainly prevented with a unit cell reduction of 10%, thus allowing to compute more meaningful values for the fabric permeability tensor.

Concerning the small influence the intra-yarn characteristics on the overall permeability, the simulations confirm, by a qualitative observation, the stronger streamlines within the inter-porosity space. So, it reveals that the relatively low intra-yarn permeability compared to the inter-yarn flow channel width is responsible for a predominant inter-yarn flow. Nonetheless, since the inter-yarn area is not always percolating, the intra-yarn flow needs to be modeled to solve the finite element problem.

One of the most important point is that the domain, including the textile modeling which has to be assessed, must be enough representative from the actual textile geometry. Avoiding the racetraking phenomenon, preferential flows, leading to an overestimation of the whole effective permeability, has to be removed. However, a permeability underestimation could also occur if the domain reduction is to high. Consequently, in our case, a 10% reduction seems to be a good trade-off.

In perspective, a further work will be devoted to compare computed permeability with experimental measurements and to extend this study to another interlock fabric. Moreover, this further work will also focus on transient flows within 3D interlock fabrics with the addition of capillary effects, that are thought to be of first importance at such low intra-yarn permeability values. Transient flow simulations will also allow to predict the location of dry areas and impregnation defects within the fabric unit cells. A numerical simulation approach will allow in this case to predict the flow with a refinement level which is very challenging to achieve experimentally. A particular interest will be given to both physical and numerical aspects occurring near the flow front and the yarn-channel numerical interface in order to precisely track the fluid velocities. Consequently, the mesoscopic and microscopic voids formation and evolution along the filling of the unit cell will be modeled and analyzed.

Acknowledgments

Authors acknowledge the support of a PhD grant N°2021/0156 from ANRT and Safran Aircraft Engines. The authors would like to gratefully thank the anonymous reviewers for their constructive comments.

References

[1] M. Ali, R. Umer, K. Khan, S. Bickerton, W. Cantwell, Non-destructive evaluation of through-thickness permeability in 3D woven fabrics for composite fan blade applications, Aerospace Science and Technology 82 (2018) 520–533.

[2] D. Rajak, D. P. Durgesh, R. Kumar, C. I. Pruncu, Recent progress of reinforcement materials: a comprehensive overview of composite materials, Journal of Materials Research and Technology 8 (2019) 6354–6374.

[3] K. Bilisik, Multiaxis three-dimensional weaving for composites: A review, Textile Research Journal 82 (2012) 725–743.

[4] N. Vernet, F. Trochu, Analysis and modeling of 3d interlock fabric compaction behavior, Composites Part A: Applied Science and Manufacturing 80 (2016) 182–193.

[5] F. M. Monticeli, D. Daou, M. Dinulovic, H. J. C. Voorwald, M. O. H. Cioffi, Mechanical behavior simulation: NCF/epoxy composite processed by RTM, Polymers and Polymer Composites 27 (2018) 66–75.

[6] A. Santos, F. Monticeli, H. Ornaghi, L. de Paula Santos, M. Cioffi, Porosity characterization and respective influence on short-beam strength of advanced composite processed by resin transfer molding and compression molding, Polymers and Polymer Composites 29 (2020) 1353–1362.

[7] T. Lundström, B. R. Gebart, Influence from process parameters on void formation in resin transfer molding, Polymer Composites 15 (1994) 25–33.

[8] M. Bodaghi, C. Cristóvão, R. Gomes, N. Correia, Experimental characterization of voids in high fibre volume fraction composites processed by high injection pressure RTM, Composites Part A: Applied Science and Manufacturing 82 (2016) 88–99.

[9] M. Yun, T. Carella, P. Simacek, S. Advani, Stochastic modeling of through the thickness permeability variation in a fabric and its effect on void formation during vacuum assisted resin transfer molding, Composites Science and Technology 149 (2017) 100–107.

[10] S. Whitaker, Flow in porous media i: A theoretical derivation of darcy's law, Transport in Porous Media 1 (1986) 3–25.

[11] E. E. Swery, R. Meier, S. V. Lomov, K. Drechsler, P. Kelly, Predicting permeability based on flow simulations and textile modelling techniques: Comparison with experimental values and verification of FlowTex solver using ansys CFX, Journal of Composite Materials 50 (2015) 601–615.

[12] Y. Xiao, J. Xu, M. Wang, B. Wang, S. Yuan, C. Yang, Multiscale model of the RTM process: From mesoscale anisotropic permeability of woven structures to macroscale resin impregnation, Industrial & Engineering Chemistry Research 60 (2021) 8269–8279.

[13] R. Arbter, *et al.*, Experimental determination of the permeability of textiles: A benchmark exercise, Composites Part A: Applied Science and Manufacturing 42 (2011) 1157–1168.

[14] N. Vernet, *et al.*, Experimental determination of the permeability of engineering textiles: Benchmark II, Composites Part A: Applied Science and Manufacturing 61 (2014) 172–184.

[15] D. May, *et al.*, In-plane permeability characterization of engineering textiles based on radial flow experiments: A benchmark exercise, Composites Part A: Applied Science and Manufacturing 121 (2019) 100–114.

[16] A. Yong, *et al.*, Out-of-plane permeability measurement for reinforcement textiles: A benchmark exercise, Composites Part A: Applied Science and Manufacturing 148 (2021) 106480.

[17] M. Bodaghi, S. V. Lomov, P. Simacek, N. C. Correia, S. G. Advani, On the variability of permeability induced by reinforcement distortions and dual scale flow in liquid composite moulding: A review, Composites Part A: Applied Science and Manufacturing 120 (2019) 188–210.

[18] M. Bodaghi, I. Gnaba, X. Legrand, D. Soulat, P. Wang, M. Deléglise-Lagardère, C. H. Park, In-plane permeability changes of plain weave glass fabric induced by tufting, Advanced Composite Materials (2020) 1–17.

[19] N. Vernet, F. Trochu, In-plane and through-thickness permeability models for three-dimensional interlock fabrics, Journal of Composite Materials 50 (2015) 1951–1969.

[20] M. A. Ali, K. A. Khan, R. Umer, An electric circuit analogy-based homogenization approach for predicting the effective permeability of complex dual-scale porous media, Materials Today Communications (2021) 102565.

[21] J. Tian, C. Qi, Y. Sun, Z. M. Yaseen, B. T. Pham, Permeability prediction of porous media using a combination of computational fluid dynamics and hybrid machine learning methods, Engineering with Computers 37 (2020) 3455–3471.

[22] B. Caglar, G. Broggi, M. Ali, L. Orgéas, V. Michaud, Deep learning accelerated prediction of the permeability of fibrous microstructures, Composites Part A: Applied Science and Manufacturing 158 (2022) 106973.

[23] A. Raizada, K. M. Pillai, P. Ghosh, A validation of whitaker's closure formulation based method for estimating flow permeability in anisotropic porous media, Composites Part A: Applied Science and Manufacturing 156 (2022) 106831.

[24] H. Teixidó, J. Staal, B. Caglar, V. Michaud, Capillary effects in fiber reinforced polymer composite processing: A review, Frontiers in Materials 9 (2022).

[25] M. Devillard, K. T. Hsiao, A. Gokce, S. G. Advani, On-line characterization of bulk permeability and race-tracking during the filling stage in resin transfer molding process, Journal of Composite Materials 37 (2003) 1525–1541.

[26] S. S. Tavares, V. Michaud, J. A. Manson, Assessment of semi-impregnated fabrics in honeycomb sandwich structures, Composites Part A: Applied Science and Manufacturing 41 (2010) 8–15.

[27] T. Cender, P. Simacek, S. G. Advani, Resin film impregnation in fabric prepregs with dual length scale permeability, Composites Part A: Applied Science and Manufacturing 53 (2013) 118–128.

[28] M. Bruschke, S. G. Advani, Flow of generalized newtonian fluids across a periodic array of cylinders, Journal of Rheology 37 (1993) 479–498.

[29] T. Papathanasiou, Flow across structured fiber bundles: a dimensionless correlation, International Journal of Multiphase Flow 27 (2001) 1451–1461.

[30] M. A. F. Zarandi, S. Arroyo, K. M. Pillai, Longitudinal and transverse flows in fiber tows: Evaluation of theoretical permeability models through numerical predictions and experimental measurements, Composites Part A: Applied Science and Manufacturing 119 (2019) 73–87.

[31] A. Geoffre, M. Ghestin, N. Moulin, J. Bruchon, S. Drapier, Bounding transverse permeability of fibrous media: a statistical study from random representative volume elements with consideration of fluid slip, International Journal of Multiphase Flow 143 (2021) 103751.

[32] E. Syerko, *et al.*, Benchmark exercise on image-based permeability determination of engineering textiles: microscale predictions, Composites Part A: Applied Science and Manufacturing (2023) 107397.

[33] M. M. B. Hasan, S. Nitsche, A. Abdkader, C. Cherif, Carbon fibre reinforced thermoplastic composites developed from innovative hybrid yarn structures consisting of staple carbon fibres and polyamide 6 fibres, Composites Science and Technology 167 (2018) 379–387.

[34] Y. Wielhorski, A. Mendoza, M. Rubino, S. Roux, Numerical modeling of 3D woven composite reinforcements: A review, Composites Part A: Applied Science and Manufacturing 154 (2022) 106729.

[35] N. Naouar, E. Vidal-Salle, J. Schneider, E. Maire, P. Boisse, 3D composite reinforcement meso F.E. analyses based on X-ray computed tomography, Composite Structures 132 (2015) 1094–1104.

[36] A. Mendoza, J. Schneider, E. Parra, S. Roux, The correlation framework: Bridging the gap between modeling and analysis for 3D woven composites, Composite Structures 229 (2019) 111468.

[37] Y. Sinchuk, O. Shishkina, M. Gueguen, L. Signor, C. Nadot-Martin, H. Trumel, W. V. Paepegem, X-ray CT based multi-layer unit cell modeling of carbon fiber-reinforced textile composites: Segmentation, meshing and elastic property homogenization, Composite Structures 298 (2022) 116003.

[38] S. Lomov, G. Huymans, Y. Luo, R. Parnas, A. Prodromou, I. Verpoest, G. Huysmans, Y. Luo, R. Parnas, A. Prodromou, Textile composites: modelling strategies, Composites Part A: Applied Science and Manufacturing 32 (2001) 1379–1394.

[39] S. Yan, X. Zeng, A. Long, Effect of fibre architecture on tensile pull-off behaviour of 3d woven composite t-joints, Composite Structures 242 (2020) 112194.

[40] D. Durville, Simulation of the mechanical behaviour of woven fabrics at the scale of fibers, International Journal of Material Forming 3 (2010) 1241–1251.

[41] D. Durville, I. Baydoun, H. Moustacas, G. Périé, Y. Wielhorski, Determining the initial configuration and characterizing the mechanical properties of 3D angle-interlock fabrics using finite element simulation, International Journal of Solids and Structures 154 (2018) 97–103.

[42] A. Mendoza, R. Trullo, Y. Wielhorski, Descriptive modeling of textiles using FE simulations and deep learning, Composites Science and Technology 213 (2021).

[43] M. A. Ali, Q. Guan, R. Umer, W. J. Cantwell, T. Zhang, Efficient processing of uct images using deep learning tools for generating digital material twins of woven fabrics, Composites Science and Technology 217 (2022) 109091.

[44] S. Blusseau, Y. Wielhorski, Z. Haddad, S. Velasco-Forero, Instance segmentation of 3d woven fabric from tomography images by deep learning and morphological pseudo-labeling, Composites Part B: Engineering 247 (2022) 110333.

[45] E. Belov, S. Lomov, I. Verpoest, T. Peters, D. Roose, R. Parnas, K. Hoes, H. Sol, Modelling of permeability of textile reinforcements: lattice boltzmann method, Composites Science and Technology 64 (2004) 1069–1080.

[46] M. W. Tahir, S. Hallström, M. Åkermo, Effect of dual scale porosity on the overall permeability of fibrous structures, Composites Science and Technology 103 (2014) 56–62.

[47] E. Syerko, C. Binetruy, S. Comas-Cardona, A. Leygue, A numerical approach to design dual-scale porosity composite reinforcements with enhanced permeability, Materials & Design 131 (2017) 307–322.

[48] Y. Chen, High-performance computational homogenization of stokes–brinkman flow with an anderson-accelerated fft method, International Journal for Numerical Methods in Fluids (2023).

[49] L. Chevalier, J. Bruchon, N. Moulin, P.-J. Liotier, S. Drapier, Accounting for local capillary effects in two-phase flows with relaxed surface tension formulation in enriched finite elements, Comptes Rendus Mécanique 346 (2018) 617–633.

[50] S. Facciotto, P. Simacek, S. G. Advani, P. Middendorf, Modeling of anisotropic dual scale flow in RTM using the finite elements method, Composites Part B: Engineering 214 (2021) 108735.

[51] Y. Song, J. Youn, Asymptotic expansion homogenization of permeability tensor for plain woven fabrics, Composites Part A: Applied Science and Manufacturing 37 (2006) 2080–2087.

[52] C. Li, J. Huang, T. Qin, C. Chen, L. Gao, J. Xu, A novel approach to simulate the resin infusion process by two phases coupling free and porous flows intra and inter fiber tows of liquid composite molding, Journal of Composite Materials 56 (2022) 3359–3367.

[53] S. Bancora, C. Binetruy, S. Advani, S. Comas-Cardona, A. Leygue, Efficient dual-scale flow simulation for resin transfer molding process based on domains skeletonization, Composites Part A: Applied Science and Manufacturing (2022) 107319.

[54] S. Badia, R. Codina, Unified stabilized finite element formulations for the stokes and the darcy problems, SIAM Journal on Numerical Analysis 47 (2009) 1971–2000.

[55] L. Abouorm, R. Troian, S. Drapier, J. Bruchon, N. Moulin, Stokes–darcy coupling in severe regimes using multiscale stabilisation for mixed finite elements: monolithic approach versus decoupled approach, European Journal of Computational Mechanics 23 (2014) 113–137.

[56] M. Blais, N. Moulin, P.-J. Liotier, S. Drapier, Resin infusion-based processes simulation : coupled stokes-darcy flows in orthotropic preforms undergoing finite strain, International Journal of Material Forming 10 (2015) 43–54.

[57] C. Li, A. Cantarel, X. Gong, A study on resin infusion and effects of reinforcement structure at dual scales by a quasi-realistic numerical simulation method, Journal of Composite Materials 54 (2020) 4157–4171.

[58] A. Geoffre, Y. Wielhorski, N. Moulin, J. Bruchon, S. Drapier, P.-j. Liotier, International Journal of Multiphase Flow Influence of intra-yarn flows on whole 3D woven fabric numerical permeability : from Stokes to Stokes-Darcy simulations, International Journal of Multiphase Flow 129 (2020).

[59] S. D. Green, A. C. Long, B. S. El Said, S. R. Hallett, Numerical modelling of 3D woven preform deformations, Composite Structures 108 (2014) 747–756.

[60] Z. Yang, Y. Jiao, J. Xie, L. Chen, W. Jiao, X. Li, M. Zhu, Modeling of 3D woven fibre structures by numerical simulation of the weaving process, Composites Science and Technology 206 (2021) 108679.

[61] M. Li, K. Liu, J. Ge, J. Xie, Z. Liu, B. Zhang, J. Huang, J. Liang, A novel modeling method for the mechanical behavior of 3D woven fabrics considering yarn distortion, Composites Science and Technology 230 (2022) 109691.

[62] H. Moustacas, D. Durville, Y. Wielhorski, Enrichissement d'une cinématique poutre. Applications aux textiles en carbone, in: 14e Colloque National en Calcul des Structures, CSMA - Giens (France) 2019, 2019, pp. 1–8.

[63] A. Trofimov, C. Ravey, N. Droz, D. Therriault, M. Lévesque, A review on the representative volume element-based multi-scale simulation of 3d woven high performance thermoset composites manufactured using resin transfer molding process, Composites Part A: Applied Science and Manufacturing 169 (2023) 107499.

[64] B. Gebart, Permeability of unidirectional reinforcements for RTM, Journal of Composite Materials 26 (1992) 1100–1133.

[65] B. Caglar, C. Tekin, F. Karasu, V. Michaud, Assessment of capillary phenomena in liquid composite molding, Composites Part A: Applied Science and Manufacturing 120 (2019) 73–83.

[66] C. Ravey, E. Ruiz, F. Trochu, Determination of the optimal impregnation velocity in resin transfer molding by capillary rise experiments and infrared thermography, Composites Science and Technology 99 (2014) 96–102.

[67] V. Michaud, A review of non-saturated resin flow in liquid composite moulding processes, Transport in Porous Media 115 (2016) 581–601.

[68] G. S. Beavers, D. D. Joseph, Boundary conditions at a naturally permeable wall, Journal of Fluid Mechanics 30 (1967) 197–207.

[69] G. Hello, J. Schneider, Z. Aboura, Numerical Simulations of Woven Composite Materials With Voxel-FE Models, in: 16th European Conference on Composite Materials (ECCM 2014), June, 2014, pp. 22–26.

[70] Z-set software, http://www.zset-software.com (2023).

[71] S. Bickerton, E. Sozer, P. Graham, S. Advani, Fabric structure and mold curvature effects on preform permeability and mold filling in the RTM process. part i. experiments, Composites Part A: Applied Science and Manufacturing 31 (2000) 423–438.

[72] MUMPS: MUltifrontal Massively Parallel sparse direct Solver, https://mumps-solver.org (2023).

[73] J. Drummond, M. Tahir, Laminar viscous flow through regular arrays of parallel solid cylinders, International Journal of Multiphase Flow 10 (1984) 515–540.